ADVANCING EARTH AND SPACE SCIENCE

JGR Earth Surface

RESEARCH ARTICLE
10.1029/2022JF006962

Key Points:

- Rainfall, wind, and lightning can be detected and distinguished with seismic data
- Seismic observations and analysis are effective for constraining debris flow characteristics such as velocity in post-wildfire environments
- Theoretical models of debris flows provide a framework to evaluate the sensitivity of seismic data to changing debris flow characteristics

Supporting Information:

Supporting Information may be found in the online version of this article.

Correspondence to:

R. Porter,
ryan.porter@nau.edu

Citation:

Porter, R., Joyal, T., Beers, R., Youberg, A., Loverich, J., Schenk, E., & Robichaud, P. R. (2023). Characterization of environmental seismic signals in a post-wildfire environment: Examples from the Museum Fire, AZ. *Journal of Geophysical Research: Earth Surface*, *128*, e2022JF006962. https://doi.org/10.1029/2022JF006962

Received 11 OCT 2022
Accepted 22 JUN 2023

Author Contributions:

Conceptualization: Ryan Porter, Taylor Joyal, Rebecca Beers, Ann Youberg, Edward Schenk, Peter R. Robichaud
Data curation: Ryan Porter, Rebecca Beers, Joseph Loverich
Formal analysis: Ryan Porter, Rebecca Beers, Ann Youberg
Funding acquisition: Ryan Porter
Investigation: Ryan Porter, Taylor Joyal, Ann Youberg, Joseph Loverich, Edward Schenk, Peter R. Robichaud
Methodology: Ryan Porter
Project Administration: Ryan Porter, Taylor Joyal
Resources: Ryan Porter, Joseph Loverich, Edward Schenk, Peter R. Robichaud
Software: Ryan Porter
Supervision: Ryan Porter, Peter R. Robichaud

Characterization of Environmental Seismic Signals in a Post-Wildfire Environment: Examples From the Museum Fire, AZ

Ryan Porter[1], Taylor Joyal[1], Rebecca Beers[2], Ann Youberg[2], Joseph Loverich[3], Edward Schenk[4], and Peter R. Robichaud[5]

[1]School of Earth and Sustainability, Northern Arizona University, Flagstaff, AZ, USA, [2]Arizona Geological Survey, University of Arizona, Tucson, AZ, USA, [3]JE Fuller Hydrology and Geomorphology, Inc., Flagstaff, AZ, USA, [4]Flagstaff Water Services, City of Flagstaff, Flagstaff, AZ, USA, [5]US Department of Agriculture, Forest Service, Rocky Mountain Research Station, Moscow, ID, USA

Abstract The 2019 Museum Fire burned in a mountainous region near the city of Flagstaff, AZ, USA. Due to the high risk of post-fire debris flows and flooding entering the city, we deployed a network of seismometers within the burn area and downstream drainages to examine the efficacy of seismic monitoring for post-fire flows. Seismic instruments were deployed during the 2019, 2020, and 2021 monsoon seasons following the fire and recorded several debris flow and flood events, as well as signals associated with rainfall, lightning and wind. Signal power, frequency content, and wave polarization were measured for multiple events and compared to rain gauge records and images recorded by cameras installed in the study area. We use these data to test the efficacy of seismic recordings to (a) detect and differentiate between different energy sources, (b) estimate the timing of lightning strikes, (c) calculate rainfall intensities, and (d) determine debris flow timing, size, velocity, and location. We then calculate forward models of seismic signals associated with debris flows and rainfall to better interpret our results and characterize these events. Our observations and modeling show that we can differentiate between these sources and that seismic data can provide insight into post-fire debris flow characteristics, including relative particle sizes and velocity.

Plain Language Summary Wildfires are a growing hazard as the size and frequency of high-severity fires are growing globally. Following containment, post-fire flooding and landslides can put downstream communities at risk, particularly as communities expand within the wildland-urban interface and close to fire-prone mountains. In this work, we use seismic instruments to measure ground vibrations created by rainfall, lightning, landslides and floods as they move downstream and compare these recordings to game camera photos and rainfall records. This data set allows us to detect and better understand hazards in post-fire areas. Observations from these instruments show a high potential for detecting these events and the validity of using seismic data as a tool for understanding debris flow behavior.

1. Introduction

Wildfires are a growing risk globally as the size and frequency of high severity events are increasing due to climate change (Abatzoglou & Williams, 2016; Jolly et al., 2015; Westerling, 2016; Westerling et al., 2006). In the western US, wildfire risk is particularly acute as a century of excessive fire suppression resulted in high fuel loads in many forests, which, when combined with climate change effects, has led to several catastrophic fires in recent years (Parks et al., 2015; Steel et al., 2015). Further, wildfires are becoming an increasing threat to people, property, and infrastructure as communities expand into the wildland-urban interface (Radeloff et al., 2018). Beyond the threat of wildfires themselves, post-fire debris flows and floods present a risk to downstream communities that can persist for years following fire containment. In this work, we analyze seismic data collected during post-fire debris flow and flood events emanating from the 2019 Museum Fire area. This fire and the landscape's post-fire response are characteristic of what we may expect following future wildfires within the southwestern United States (Sankey et al., 2017). We use these data to test the efficacy of using seismic instruments and analysis techniques to characterize post-fire debris flows beyond event detection. We then compare our observations to forward models of debris flow seismic signals to test the data sensitivity to changes in debris flow characteristics, such as particle size.

Visualization: Ryan Porter
Writing – original draft: Ryan Porter
Writing – review & editing: Taylor Joyal, Rebecca Beers, Ann Youberg, Joseph Loverich, Edward Schenk, Peter R. Robichaud

The Museum Fire, located in the Dry Lake Hills and Mount Elden immediately north of Flagstaff, AZ (Figure 1) ignited 21 July 2019 during an abnormally dry monsoon season due to a rock strike by heavy equipment during forest thinning activities (Museum Fire BAER Team, 2019). The fire occurred in ponderosa pine (*Pinus ponderosa*) and mixed conifer forest at elevations between ~2,200 and ~2,750 m. Full containment was achieved on 12 August 2019 with an estimated burned area of ~8 km^2. Post-fire assessment of the burn area estimated that 12% of the soil burn severity was very low, 48% was low, 28% was moderate, and 12% was high (Figure 2; Museum Fire BAER Team, 2019). Most of the burn area drains into the Spruce Wash Watershed (SWW), an ephemeral drainage that flows through communities in eastern Flagstaff. The watershed is located on mountainous terrain comprised of Pleistocene-age dacitic lava domes with steep flanks (Holm, 1988; Figure 1). It is susceptible to post-fire flooding due to its steep slopes, vegetation loss due to fire, and increased soil hydrophobicity (see Porter et al., 2021, Supplemental Sheet 2 for infiltration measurements). Alluvial C14 chronology from the Schultz Creek Watershed, an adjacent watershed, shows that sediment has been accumulating in the ephemeral channel for approximately 7,000 years without major fires or flooding (Stempniewicz, 2014). Regional channel geometry observations support this chronology, with the majority of bankfull channel area in forested watersheds being undersized for the area of the watershed indicating complacent rainfall-runoff conditions (Schenk et al., 2021). A similar absence of recent fire and flooding is also expected for the SWW prior to the Museum Fire, leaving significant quantities of sediment available to mobilize during storms after the 2019 fire.

Northern Arizona's climate makes it susceptible to post-fire debris flows and flash flooding. The climate is characterized by four distinct seasons, a cold snow-dominated winter, a dry and windy late-spring/early summer, a wet late summer, and a temperate fall. Most of the region's precipitation occurs during the winter, in the form of snow, and in summer, when convective monsoonal storms occur (Jurwitz, 1953). Wildfire season typically extends from late May to early July, when conditions are commonly dry, hot, and windy. However, from July to September, precipitation from monsoonal storms raises the soil moisture and lowers the region's fire risk (Nauslar et al., 2019). These summer convective storms are characterized by high intensity, short-duration rainfall events that can produce flash-flooding even in unburned terrain (Adams & Comrie, 1997). When these storms occur over recently burned hydrophobic soils, the risk of post-fire runoff (i.e., debris flows and flooding) is greatly increased (DeBano, 2000). Climate change projections for the southwestern United States predict drier conditions, reduced snowpack, higher temperatures, and increased extreme weather events (Barnett et al., 2005, 2008; Brown et al., 2004; Cook et al., 2004). These changing conditions will likely lead to increased wildfire frequency and severity across the region, as well as extreme weather events, which together increase the likelihood of catastrophic mass-wasting events (e.g., Sankey et al., 2017; Touma et al., 2022; Westerling et al., 2003; Yue et al., 2013).

The occurrence of monsoonal storms immediately following wildfire season makes Arizona extremely susceptible to post-fire flooding (Staley et al., 2020). This risk is particularly acute when wildfires occur in regions of steep topography adjacent to population centers. For the Museum Fire, the high likelihood of flooding and debris flows from the burn area and the proximity to a population center led us to deploy a network of seismometers and other monitoring equipment to detect and characterize these events. The 2019 monsoon season was the driest on record at the time until it was surpassed by the 2020 season. Because the 2019 and 2020 monsoon seasons were abnormally dry, only a few convective storms occurred, which produced few debris flows and flood events. Damage from these events was limited to USDA (United States Department of Agriculture) Forest Service land. During this time, field saturated hydraulic conductivity decreased within the study area (Porter et al., 2021). The 2021 monsoon season was substantially wetter than average, and several major high-intensity storms occurred during July and August (Table S1 in Supporting Information S1). These storms triggered multiple episodes of flooding and debris flows. These debris flows repeatedly caused significant damage to the main Forest Service road to the area, but were limited to Forest Service lands. However, flood flows continued downstream, impacting numerous properties and buildings within the City of Flagstaff, including an elementary school.

Post-fire debris flow detection and monitoring present observational challenges. It is difficult to predict when and where convective precipitation will occur within a large burned area and where slopes will destabilize. Currently, monitoring of post-fire debris flows is done using a combination of cameras, rain gauges, non-contact stage gauges, and seismic equipment to estimate for debris flow and flood timing (e.g., Kean & Staley, 2011; McGuire & Youberg, 2020; McGuire et al., 2018; Michel et al., 2019; Raymond et al., 2020; Tang et al., 2019). Beyond event detection, seismic monitoring is a promising tool that can supplement these observations and allow us to better understand debris flow behavior and flood initiation conditions and track propagation through

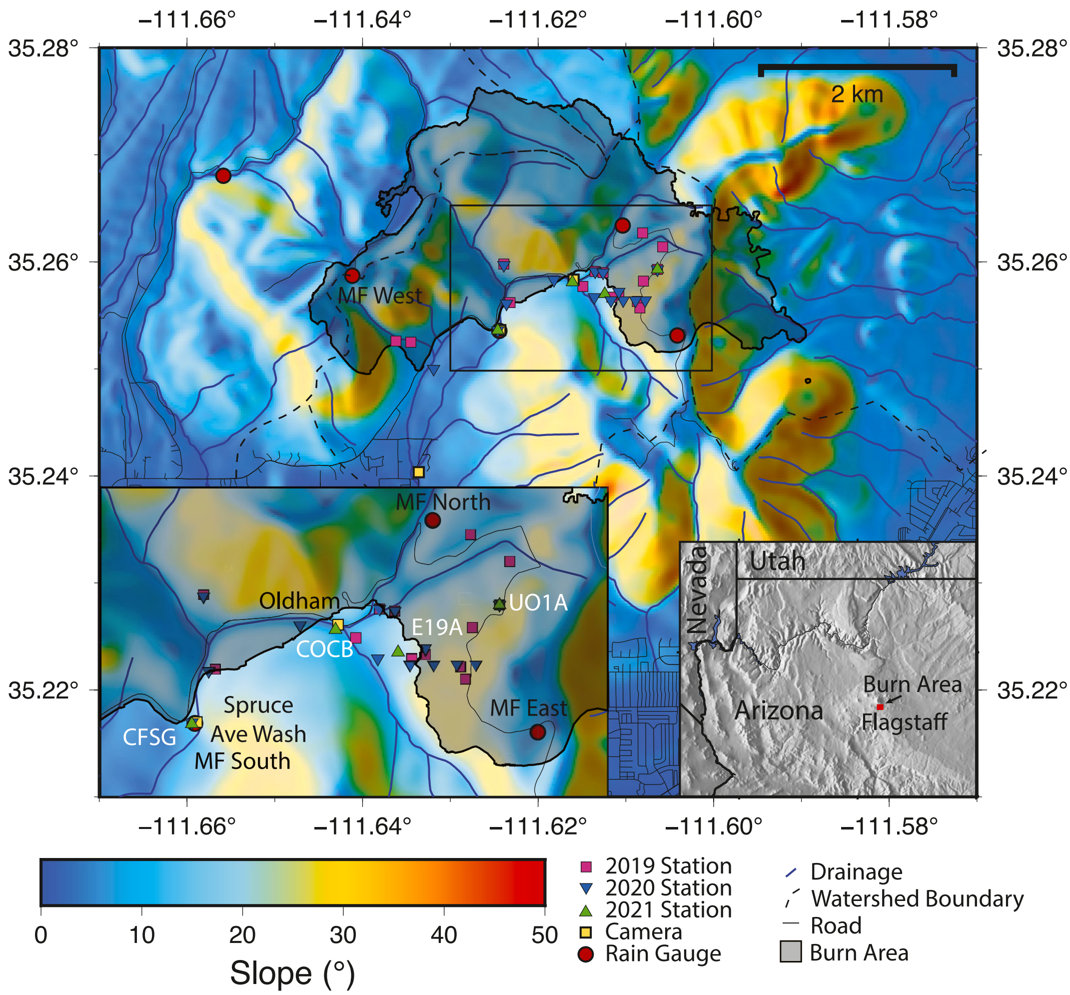

Figure 1. Location map of the study area showing the burn area (shaded gray), seismic station locations, rain gauges, camera locations, drainages, and watershed boundaries. Colors indicate slopes.

a watershed. These observations are ideal for this purpose as the instruments are designed to work in a range of extreme weather conditions, are unaffected by light levels, record debris flow energy from 10 to 100s of meters away in most cases, and do not have to be located within or aimed at a specific hillslope or segment of channel. Further, these instruments are frequently telemetered from remote locations with a latency of <1 min between data collection and public availability (Benson et al., 2012; Trabant et al., 2008). There is a growing body of theoretical work that provides insight into the sensitivity of these data to debris flow characteristics and gives us a framework to interpret these data.

The use of seismic monitoring for detecting and characterizing debris flows is part of a recent expansion in the use of seismic analyses for non-traditional applications. These applications include using seismic data to monitor surface processes including estimating bed load in rivers and characterizing mass wasting events (Bessason et al., 2017; Burtin et al., 2008, 2009, 2011, 2013, 2014; Cornet et al., 2005; Coviello et al., 2019; Ekstrom & Stark, 2013; Kean et al., 2015; Lai et al., 2018; Marineau et al., 2019; Roth et al., 2014, 2016; Schmandt et al., 2013; Suwa et al., 2011; Tsai et al., 2012; Walter et al., 2017). In this work, we apply and build on previous theoretical and observational work applying seismic observations to better understand debris flow properties (Allstadt, 2013; Allstadt et al., 2020; Bessason et al., 2017; Coviello et al., 2019; Farin et al., 2019; Kean et al., 2015; Lai et al., 2018; Zhang et al., 2021).

The primary source of seismic energy during debris flows and floods is the collision of sediment particles with the channel bed (Kean et al., 2015; Lai et al., 2018; Tsai et al., 2012). Theoretical work shows that the amplitude and frequency content of a debris flow seismic signal is controlled by a combination of flow properties, the nature of the impacts, distance from the seismic instrument, channel properties, and subsurface properties. Debris flow

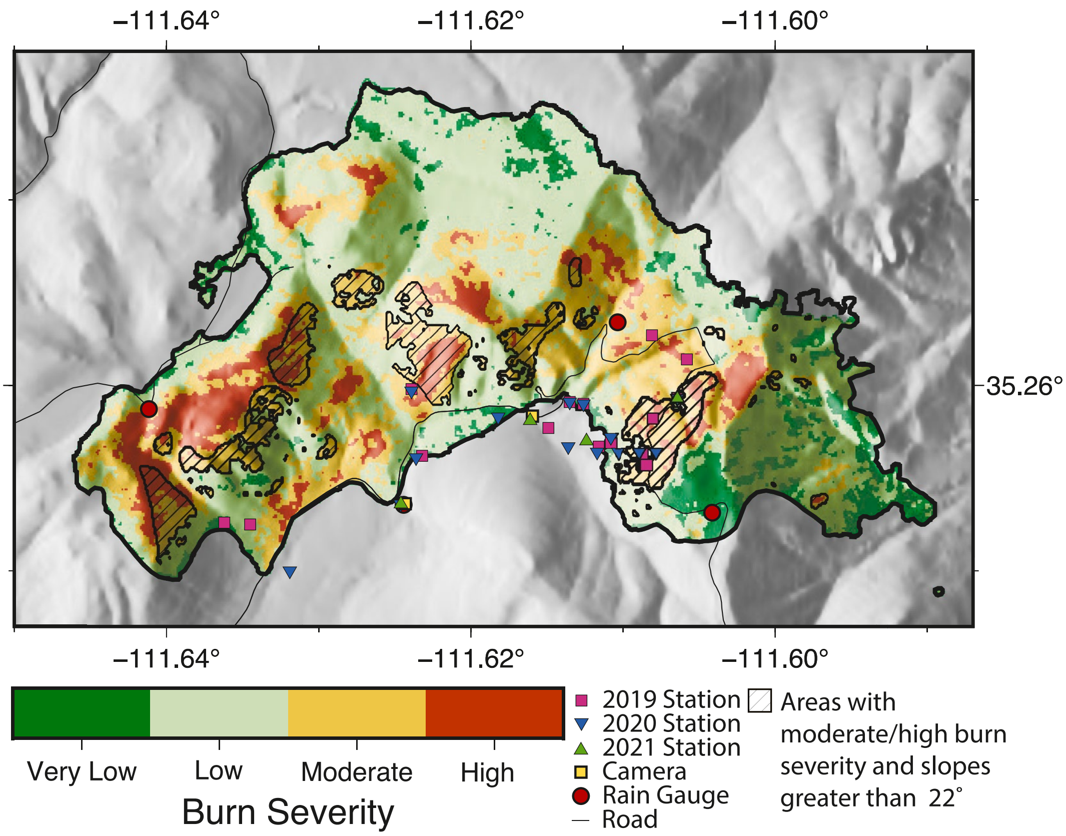

Figure 2. Burn severity map for the Museum Fire (Museum Fire BAER Team, 2019; Figure 1). Shaded area denotes areas with moderate to high severity burn designations and slopes greater than 22° where debris flows are most likely.

properties include particle size and density, flow area (length and width), flow depth, velocity, and the ratio of solids to liquid within the flow (Farin et al., 2019; Lai et al., 2018; Roth et al., 2016; Tsai et al., 2012). Of these factors, debris flow velocity, flow size, particle size, distance from the station, and channel and subsurface properties have the greatest impact on the observed signal (Farin et al., 2019). Many of these properties can be constrained by assessing the geometry of the channel adjacent to a seismic station and analyzing the frequency content of the signal. This leaves velocity and grain size as the most impactful unconstrained controls on the seismic signal (Farin et al., 2019). In the following sections, we discuss how we can constrain these factors to better understand post-fire debris flows, floods, and other seismic signals in post-fire environments.

2. Data and Methods

Seismic instruments were deployed to detect and characterize debris flows for three summers following the Museum Fire (2019, 2020, and 2021). Stations consisted of either L-22 short period instruments deployed using IRIS PASSCAL quick deployment boxes or Nanometrics Meridian Compact 120s systems (3 dB corners at 120 s and 108 Hz). In 2019 and 2020, 15 and 12 instruments were deployed, respectively, in arrays designed to record events in as many drainages as possible. All seismic data and station metadata are archived at the IRIS DMC (Data Management Center) and a summary of the data and its availability for the 2019 and 2020 deployments is described in Porter et al. (2021). In 2021, efforts were scaled back with only four Nanometrics instruments deployed for the monitoring efforts. These four stations were installed along the main drainages within the burn area. We deployed two in the upper watershed, and two in the lower watershed along the main stem of the SWW (Figures 1 and 2). Though we record multiple flood and debris flow events, we focus our current analyses on the multiple debris flows recorded at station E19A located in the upper watershed from the 2021 monsoon season.

In addition to seismometers, a network of cameras and rain gauges were also installed within the burn area for debris flow and flood detection and early warning (Figures 1 and 2). The camera network consisted of four telemetered cameras and six non-telemetered cameras. These cameras were aimed at the drainages where flooding was considered likely and are used to corroborate our seismic observations. Three tipping bucket rain gauges, which transmit data in real time at 0.04″ rain intervals, were installed within the burn area. Additionally, an existing rain and stream gauge within the burn area was upgraded after the fire. These gauges are part of a larger publicly available rain network operated by the City of Flagstaff consisting of 37 gauges designed to identify flood risks during monsoonal storms in the Flagstaff vicinity (Schenk et al., 2021).

We compare seismic data to rain gauge and radar observations to better constrain debris flow initiation timing and behavior. We identify major rain events using data from four rain gauges located within the burn area. Based on observations from the 2019 and 2020 monsoon seasons, debris flows were deemed likely to occur during events that had 15-min intensities greater than 30 mm/hr or 60-min intensities greater than 15 mm/hr. Table S1 in Supporting Information S1 lists every storm that met at least one of those criteria at a minimum of one rain gauge within the burn area. Storm start times and durations are based on the timing that these thresholds are first and last exceeded by any gauge within the array. This highlights the localized nature of these convective monsoonal storms as extreme variations in rain intensity and storm total are observed over spatial scales of hundreds of meters to a few kilometers. For example, rain gauges Museum Fire North and Museum Fire East are located ∼1 km apart and, in most storms, recorded significantly different peak intensities and total rainfall amounts.

Data from the National Weather Service Doppler-radar station (Next Generation Weather Radar [NEXRAD], WSR-88D) KFSX, located ∼75 km south-southeast of Flagstaff, were integrated with gauge data to more accurately estimate the spatial extent and quantity of rainfall derived from radar data. To accomplish this, level-3 NEXRAD base reflectivity data, collected at a 0.5-degree angle, were downloaded and compared to rain intensities recorded at the rain gauges. A non-linear least squares fit was used to calculate the power law relationship between radar reflectivity (Z in mm^6 m^{-3}) and rainfall intensity (R in mm hr^{-1}) by solving for a_r and b_r in the Z-R relationship equation (e.g., Marshall et al., 1947):

$$R = \left(\frac{1}{a_r}\right)^{(1/b_r)} Z^{(1/b_r)} \tag{1}$$

for each storm. This was accomplished by calculating intensity at 5-min increments at each rain gauge and comparing these to radar power (Z) for the same time period and location. Using all Z and R data available, we determine a_r and b_r values for each storm using non-linear least squares fit for Z values less than 60 db. In this fit, data were weighted by the inverse of the distance from the center of the Museum Fire burn area to ensure that rainfall estimates were most consistent with rain gauge data in the study area. Using the calculated a_r and b_r values for each storm, radar-derived intensities were summed to calculate rainfall totals. Rainfall amounts and intensities from radar were then compared to the timing of debris flow initiation determined from seismic data.

2.1. Seismic Processing

Seismic data were processed to assess the efficacy of purpose-built arrays for characterizing post-fire debris flows beyond event detection. Data were archived at the IRIS DMC and downloaded for debris flows that occurred during the 2021 monsoon season. Raw data were tapered, detrended, demeaned, and filtered between 1 and 99 Hz, and the instrument correction was applied to transfer the signal to ground velocity using the IRIS DMC data services. The data were then downloaded and resampled from 500 to 200 Hz to focus analyses on the frequency bands where the seismometers are most sensitive. To better quantify the seismic signal associated with debris flows and differentiate between sources, we calculated signal power and short-time Fourier transforms of the processed data to generate spectrograms of the signals. Using these short-time Fourier transforms, we estimate the peak frequency (f_{max}) and spectral centroid (f_{cent}) over a moving window to assess how these observations and wave polarizations change based on the type of seismic source.

Wave polarization characteristics were calculated to better differentiate between energy sources using the following equations (Jones et al., 2016; Jurkevics, 1988; Vidale, 1986):

$$P = 1 - \left(\frac{2\lambda_3}{\lambda_1 + \lambda_2}\right) \tag{2}$$

$$I = \left(\frac{\sqrt[2]{\mathrm{Re}\left(v_{12}^2\right) - \mathrm{Re}\left(v_{13}^2\right)}}{\mathrm{Re}(v_{11})}\right) \tag{3}$$

$$\theta = \left(\frac{\mathrm{Re}(v_{13})}{\mathrm{Re}(v_{12})} \right) \tag{4}$$

where P is planarity, I is incidence angle, θ is the azimuth, and λ_i and v_{ij} are the eigenvalues and eigenvectors for a time window, respectively (Table S2 in Supporting Information S1). The variables i and j can equal 1, 2, or 3 and represent the different eigenvalues and the three components of the eigenvectors in the coordinate frame, respectively. Planarity values can range from 1 to 0, with 1 representing a wavefield polarized into a plane and 0 representing a wavefield with motion equally distributed in three directions. Incidence angle and azimuth range from −90° to 90° and 0° to 180°, respectively, and give insight into the orientation of the first eigenvector. This provides information into the orientation of ground motion, which is useful for discerning the source of the seismic signals.

2.2. Seismic Modeling

We calculate synthetic models of the seismic signal power and spectral content associated with noise, rainfall, and debris flows to better interpret our results. These are based on existing theoretical frameworks for seismic signals generated by surface processes. Though we do not attempt to match our observed data exactly, these calculations are useful for providing context to our observations and for exploring the seismic response to variations in debris flow and subsurface properties, and the relative contributions of rain, noise and debris flows to the overall seismic signal.

Approximations of background noise, much of which is likely due to wind interacting with trees, are calculated using recordings of the seismic signal in the hours preceding storms. We transform these data to the frequency domain where we apply a spline interpolation to calculate frequency envelopes of these data. We select random amplitudes in the frequency domain between the frequency envelope minimum and maximum values. These values are then inverse Fourier transformed back to the time domain. This results in a pseudo-random signal with a frequency content and amplitude similar to the background noise observed at the seismic station. This signal is input as the background signal in our synthetic models to represent noise.

2.3. Rainfall Modeling

To model rainfall, we follow a similar methodology to Bakker et al. (2022), where we assume spatially uniform rainfall in the vicinity of the instrument. This modeling allows us to explore the effect of rain on the observed seismic signal and demonstrates that rainfall intensity can be estimated using seismic data. For reasonable rain drop size of 0.1–8 mm, an impact should occur over less than 0.001 s and can be assumed as an infinite frequency source for seismic purposes. We calculate the signal power density (PSD) as a function of frequency (f) using the equation:

$$\mathrm{PSD}(f) = (2\pi f)^2 \int_0^{\infty} 2\pi J_p G(f,r)^2 dr \tag{5}$$

where r is the distance from the station, J_p is the impulse flux, and $G(f,r)$ is the Green's function.

We calculate impulse flux by summing the impact forces for a distribution of raindrop sizes described by $p(d)$ using the following equation:

$$J_p = \left(\frac{4}{3} \pi \rho_w \right)^2 \gamma \sum (0.5 p(d))^6 v(p(d))^2 \tag{6}$$

where d is drop diameter, ρ_w is the density of water, γ describes the elasticity of the impact, and $v(p(d))$ is the velocity of drops as a function of diameter. We assume an inelastic impact with the ground, which gives us a γ value of 1. We estimate $p(d)$ to calculate the impact rate per unit area following (Uijlenhoet & Stricker, 1999) where raindrop size distribution is a function of rain intensity.

$$p(d) = \frac{\Lambda^{1+\beta}}{\Gamma(1+\beta)} d^B e^{-\Lambda d} \tag{7}$$

where $\Lambda = 4.1\ \mathrm{R}^{-0.21}$, R, is rainfall intensity, Γ is the gamma function, and $\beta = 0.67$ (Uijlenhoet & Stricker, 1999).

Drop velocity is calculated as $v(d) = ad^B$ (Atlas & Ulbrich, 1977) with constants a and B equal to 3.778 and 0.67, respectively (Uijlenhoet & Stricker, 1999). In this relationship, we set 9.5 m/s as the maximum raindrop velocity (Bakker et al., 2022). This assumption has little effect on the results, as even at high intensities where large drops are expected, few rain drops are large enough to exceed this velocity.

2.4. Green's Function

Surface waves are expected to dominate the observed environmental signals, so we use a near-field approximation of the Rayleigh wave Green's function (Aki & Richards, 2002; Bakker et al., 2022; Gimbert et al., 2014), which is calculated as follows:

$$G(f,r) = N_{jz}\frac{f}{8p_0 v_c^2 v_u}\left(1+\left(\frac{\pi^2 f r}{v_c}\right)^3\right)^{\frac{-1}{6}} e^{\frac{-\pi f r}{v_u Q}} \tag{8}$$

where f is frequency, ρ_0 is the density at the surface, v_c is the phase velocity, v_u is the group velocity, r is the source-receiver distance, Q is the quality factor, and N_{jz} is a unitless value that described the relative amplitudes of the three components (the z subscript indicates the vertical component). At high frequencies, where rain is observed seismically, N_{jz} is near unity (Tsai & Atiganyanun, 2014), so we assumed a value of 1 for rain. Phase (v_c) and group velocities (v_u) are calculated for Rayleigh waves following Tsai and Atiganyanun (2014) where:

$$v_c(f) = v_{c0}\,(f/f_0)^{-\xi} \tag{9}$$

$$v_u(f) = v_c\,(f)^{(1+\xi)} \tag{10}$$

where ξ describes the velocity change with depth, f_0 is a reference frequency set to 1 Hz and v_{c0} is a reference phase velocity.

2.5. Debris Flow Modeling

Debris flow signal power was calculated using an equation to estimate seismic energy for a thin flow (Farin et al., 2019):

$$\mathrm{PSD}(f,r,D) = \int (2\pi f)^2 {N_{jz}}^2 {I_j}^2 R_{\mathrm{impact}} W\, G(f,r)^2 dr \tag{11}$$

where f is frequency, r is distance from the station to points along the channel, W is channel width, and G is the Green's function defined above. R_{impact} is the impact rate calculated as $R_{\mathrm{impact}} = \frac{u_x \phi p(D)}{D_b D^2}$ where u_x is the velocity of the flow, ϕ is fraction of the flow volume that consists of solids, $p(D)$ is the grain size distribution, D_b is the bed bump-diameter, and D is grain size. The impulse I_j is defined as $I_j = (1+e_b)u_x m f_j$, where e_b is the basal coefficient of restitution, m if the particle mass, an f_j is a unitless value related to speed change during particle impact.

Assuming a linear channel oriented in the x direction located at a distance r_0 from the station at its closest point and the same Green's function as above. This equation becomes

$$\mathrm{PSD}(f,r_0,x,D) = R_{\mathrm{impact}} W {N_{jz}}^2 {I_j}^2 \frac{\pi^4 f^4 (1+e_b)^2 m^2 {u_x}^2 r_0}{4{p_0}^2 {v_c}^4 {v_u}^2} \int_{x_{\min}/r_0}^{x_{\max}/r_0} \left(1+\left(\frac{\pi^2 f r_0\sqrt{1+y^2}}{v_c}\right)^3\right)^{\frac{-1}{3}} e^{\frac{-2\pi f r_0\sqrt{1+y^2}}{v_u Q}} dy \tag{12}$$

where $y = \frac{x}{r_0}$ and $x = 0$ at the closest point in the channel to the station.

We follow previous work and use a log-raised cosine grain size distribution (Farin et al., 2019; Tsai et al., 2012) with a standard deviation of 0.5 to calculate the grain size distribution ($p(D)$) of the flow, which is input for D in Equation 11.

Rather than assume a constant grain size (D_{50}) for the snout and body of the debris flow, we calculate D_{50} grain size as a function of x and x_{max}, which is the location of the front of the debris flow, by combining a decay function with a decaying sine function (Figure S1 in Supporting Information S1):

$$D_{50(x)} = 0.05 + 0.1\, e^{-0.01\left(\frac{x_{\max}}{r_0}-y\right)} + 0.2\, e^{-0.1\left(\frac{x_{\max}}{r_0}-y\right)}\left(\frac{2\pi r_0}{x}\left(\frac{x_{\max}}{r_0}-y\right)\right) \quad (13)$$

While we do not attempt to match the exact observed signal, this grain size equation was chosen to simulate short duration increased signal power due to pulses of coarse grain sediment moving down the channel and the overall decay in the signal power in the observed data. The inputs to the model and their rationales are presented in Supporting Information S1 (Table S3).

3. Results and Discussion

Seismic records from our deployment allow us to better understand the seismic signal produced by debris flows and affirm the efficacy of seismic monitoring for estimating debris flow properties beyond timing in post-fire settings. During monsoonal storms, we commonly observe signals associated with wind, lightning, storm precipitation, and storm-induced debris flows and flood flows. Each signal is associated with distinct signal powers, frequency content, and ground motion polarizations. We show ground velocity, signal power, and spectrograms for vertical component seismic data in both our synthetic and observed data, though the signals can also be observed in the horizontal components. In Figures 3–6, the top panels (a) show the ground velocity at the seismic station E19A and panels b shows the total signal power. Panels c are spectrograms calculated using short-time Fourier transforms. These are heat maps of the signal frequency content with time, allowing for a determination of which frequencies are observed for different sources. The f_{max} and f_{cent} (panels d) values summarize this frequency content. Panels e are measures of particle (ground) motion, which summarize how the earth moves at the station with time. In analyzing these seismic signals, we can use their characteristics to differentiate between the different sources, estimate the timing of lightning strikes, rainfall intensity, rainfall kinetic energy, and debris flow timing, velocity, and location.

The seismic signal from wind is frequently site specific and can vary over short spatial scales due to differences in aspect, vegetation, and infrastructure (Johnson et al., 2019). To explore the site-specific wind signal, we use seismic recordings of windy days in the early summer where no precipitation occurred. Figure 3 shows the seismic signal observed on 27 June 2021 when wind speeds recorded at the Flagstaff airport between 10:00 and 18:00 hr, local time, ranged between 10 and 13.2 m/s with a maximum gust of 23.2 m/s (Visual Crossing Corporation, 2022). At site E19A, located in the upper watershed, we observe wind as a low frequency signal ($f_{max} < 20$ Hz) on that day. The mean signal power during that recording period was ∼−142 dB, which is substantially lower than signal powers associated with lightning, precipitation, and debris flows. Energy polarization of wind recordings at E19A shows variable azimuthal directions, planarity values of ∼0.65, and incidence angles near horizontal. The polarizations are consistent with what would be expected from the signal stemming from trees located at all azimuths from the station vibrating in the wind.

Lightning is observed as impulsive, short duration (generally <10 s) signals that excites a wide range of frequencies (Figure 4). These are most easily observed prior to debris flow and rainfall signals. We compare seismic recordings to records of lightning strikes from National Lightning Detection Network (NLDN; Cummins & Murphy, 2009; Murphy et al., 2021; Orville, 2008). Seismic detection of lightning is likely impacted by topography and atmospheric conditions. Lightning tends to have high incidence angles and variable planarity and azimuth values associated with it (Figure 4). These orientations are consistent with lightning strikes dispersed in all azimuths from the station and a vertically polarized signal. It is distinguishable from rain due to its short duration, frequency content, and high amplitudes.

During storms, we commonly observe relatively high frequency (>50 Hz) signals due to precipitation (Figures 5 and 6). The amplitudes of these signals correlate temporally with estimates of rainfall intensity observed at nearby rain gauges. However, given the highly localized nature of monsoonal storms in the southwestern US (Table S1 in Supporting Information S1), if the instruments are not co-located, there is often a lag between seismic and rain gauge observations associated with storms moving across the landscape. Although not as accurate

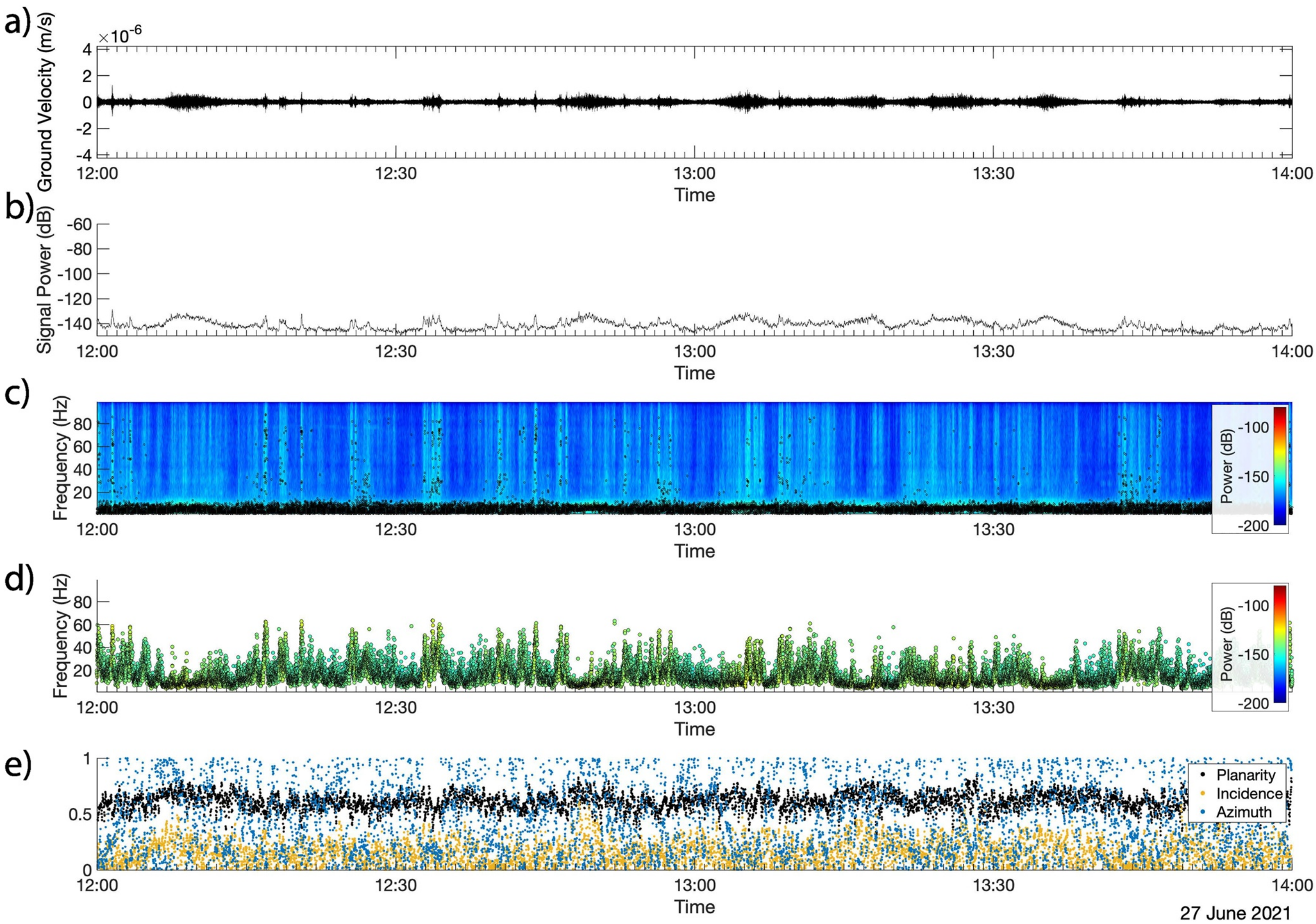

Figure 3. Seismic recording of wind at station E19A. Panel (a) shows ground velocity. Panel (b) shows decibel signal power measured between 1 and 99 Hz. Panel (c) is a spectrogram of the seismic velocity with colors indicating the signal power at the frequency shown on the *y*-axis. Signal power is calculated using a short-time Fourier transform over 0.5-s windows. Black diamonds indicate the frequency with the maximum energy (f_{max}) for each 0.5 s time window. Panel (d) shows the spectral centroid (f_{cent}), color indicates the total signal power. The spectral centroid is the weighted average short-time Fourier transform over each time window. Panel (e) shows the planarity, the absolute value of the cosine of incidence angle (0 is horizontal and 1 is vertical), and the normalized azimuth of the signal between 0 and 180°, where 0 is equal to 0° (due North) and 1 is equal to 180° (due south). No rainfall occurred during this time period.

as dedicated rain gauges, given the ease of installing seismic instrumentation, these data could be a useful tool for estimating spatial variations in rainfall across a burn area. Theoretically, the seismic signal of rain is controlled by the Green's function, rain drop quantity, and drop size distribution (which also controls the distribution of drop velocities; Bakker et al., 2022). Peaks in seismic signal power correlate well with increases in rainfall intensity (R) at nearby rain gauges. For station E19A, polarization analysis shows that rainfall has high incidence angles, moderate (~0.5) planarity, and variable azimuths, which is consistent with measurements of rainfall recorded at other stations. Energy polarization is consistent with near vertical impacts and sources dispersed at all azimuths from the station. The high frequency content of the signal is due to the proximity of rainfall to the station. Work by Bakker et al. (2022) shows that, due to signal attenuation, over half of the energy observed at a station due to rainfall comes from raindrops within 10 m of the station and 90% from drops within 25 m.

Debris flows are observed as high amplitude signals that may excite a range of frequencies (Figures 5 and 6). The signal power at a station increases rapidly as the debris flow approaches the station and then gradually decreases as the flow velocity and grain size decrease over time. Consistent with theoretical work, the frequency content of these flows appears to be controlled by the distance between the station and the debris flow and subsurface properties (i.e., the Green's function; Farin et al., 2019; Lai et al., 2018). We observe a decrease in seismic frequency (f_{max} and f_{cent}) as the seismic signal from the snout of the flow is first recorded at the station. This is followed by an increase as the snout gets closer to the station, which is consistent with signal frequency content dominated by attenuation (Farin et al., 2019; Lai et al., 2018; Tsai et al., 2012). The initial decrease in f_{max} and

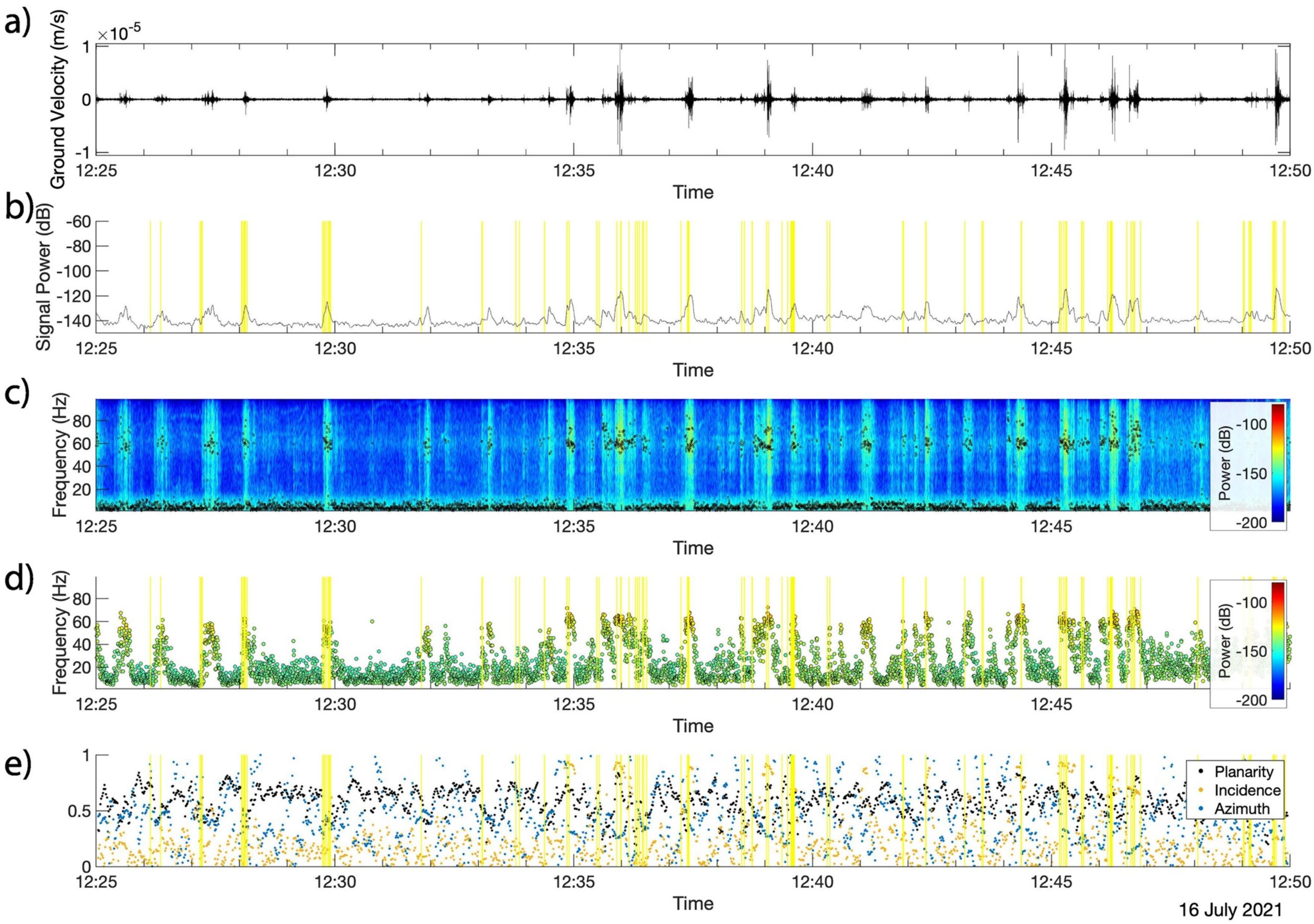

Figure 4. Seismic recording of lightning at station E19A. Panels are the same as Figure 3, except the amplitude scale in panel (a), vertical yellow lines in panels (b, d, and e). These lines indicate lightning strikes from the National Lightning Detection Network (NLDN) occurring within 12 km of the station. Lightning times are displayed at the estimated arrival time of the energy at the station using the NLDN lightning locations and timings and assuming a velocity of 330 m/s. No rainfall occurred during this time period.

f_{cent} is likely due to the increased contribution of the debris flow to the seismic signal relative to rain, wind, and other background noise. Alternately, this signal may be due to an increase in water flow within the channel, which commonly produces a lower frequency signal than particle collisions with the channel bed (e.g., Gimbert et al., 2014; Schmandt et al., 2013). Flowing water produces a seismic signal due to water/channel interactions and turbulence within the flow. This seismic signal was previously documented in large turbulent rivers and it is unclear how significant this signal would be given the relatively small size of the drainage and flows in the study area. Once the debris flow is near the station, it is several times higher amplitude than the rain and wind signals and dominates the observed signal. Within individual debris flows, we observe multiple changes in frequency content and signal power over short periods of time. Values measured for f_{max} and f_{cent} often exhibit a sawtooth pattern. These changes in amplitude and frequency content are likely due to a combination of coarse-grained particles and high-velocity flows moving through the system and approaching the seismometer. Similar patterns are observed at station UO1A during debris flows too, affirming it not just occurring at E19A. The peaks in amplitude and f_{max} occur when coarse sediment is in closest proximity to the station.

In Figures 5 and 6, we show records of two storms and associated debris flows recorded at station E19A, located in the steeper upper watershed (Figure 1). This station was installed ~20 m north of a drainage that was deemed likely to experience debris flows. As an example of the data recorded at this station, on 16 July 2021 we observed two separate debris flows in a short period between 13:00 and 14:00 hr local time. Prior to the flows, we observe several lightning strikes (Figure 4) followed by a signal we associate with rainfall. Rainfall intensity at the Museum Fire north gauge peaked at ~13:14, which coincides temporally with a peak in high frequency seismic energy (>50 Hz) at the station. At 13:16, a low frequency signal (<20 Hz) is first recorded that is likely caused

10.1029/2022JF006962

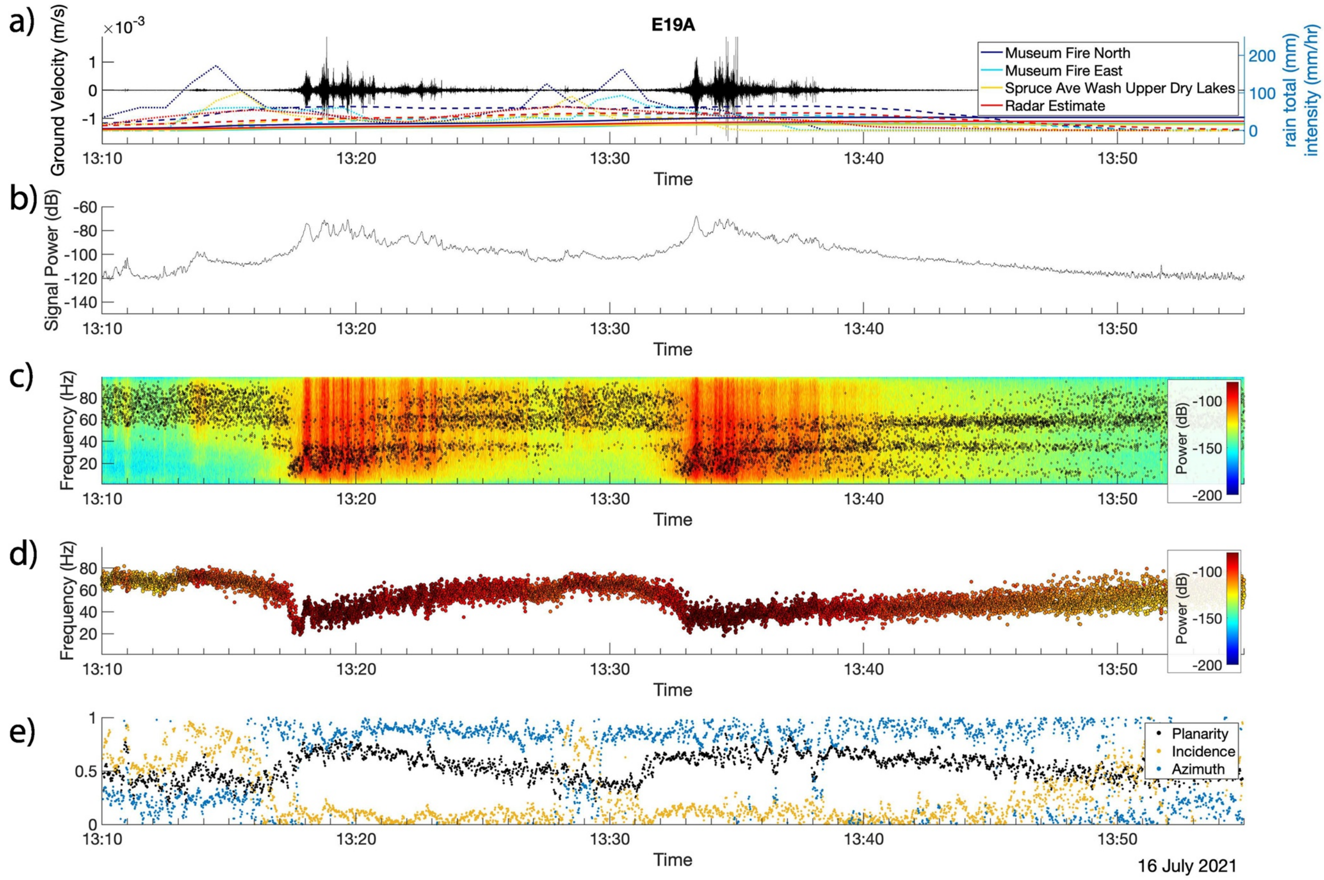

Figure 5. Seismic recording of debris flows at station E19A on 16 July 2021. Panels are the same as Figure 3, except for panel (a) which has a different amplitude scale and now shows storm rainfall total (solid line), 15-min rainfall intensity (dashed line), and 1-min intensity (dotted line). The 1-min intensity values are shown to compare seismic observations to real-time rain intensity.

by flow in the channel. There is also a higher frequency signal (>30 Hz) observed at this time from an ambiguous source. The energy that produced this signal may be from sediment transport in the channel; however, we would not expect the "gap" in energy at ∼20–25 Hz that occurs from 13:16 to 13:17 or an f_{max} with a higher frequency than observed when the debris flow snout is in closest proximity to the station if that was the case (Figure 5c). Alternately, this seismic signal was possibly caused by sheet flow on the hillslope near the station, which would result in a higher frequency signal due to the proximity of the station to the flow.

The low frequency signal, first observed at 13:16, begins increasing in amplitude and frequency at ∼13:17 (Figure 5). This is likely due to the snout of the debris flow approaching the station. This signal peaks in amplitude just after 13:18, which is when the snout reaches its closest point in the channel to the station. Following the initial debris flow snout signal, we observe multiple high amplitude pulses between 13:18 and 13:24. These signals produce a sawtooth pattern in the observed f_{max} and f_{cent} values. These power and frequency patterns are likely due to multiple pulses of coarse sediment or high-velocity flow, separated by finer grained or slower flow, traveling down the channel. After the initial high amplitude signal, the overall amplitude of the debris flow signal power decreases, which is likely due to decreases in discharge, velocity, and/or grain size. The debris flow produces the largest signal power at the station until ∼13:27 when an increase in rainfall intensity occurs. This change in signal source is inferred based on a change in frequency content and energy polarization that occurred at that time. Rainfall is the highest amplitude signal until ∼13:29 when a second debris flow is observed in the seismic data. The signal from this second flow is similar to the first. It exhibits increased signal power initially followed by multiple pulses of increased amplitudes and sawtooth changes in f_{max} and f_{cent}. After peaking, this signal gradually decays back to baseline (pre-storm) values.

On 17 August 2021, we observe a similar signal to the 16 July events (Figure 6) at station E19A, demonstrating the consistency of debris flow signals recorded at the station. For this August debris flow, a remote game camera

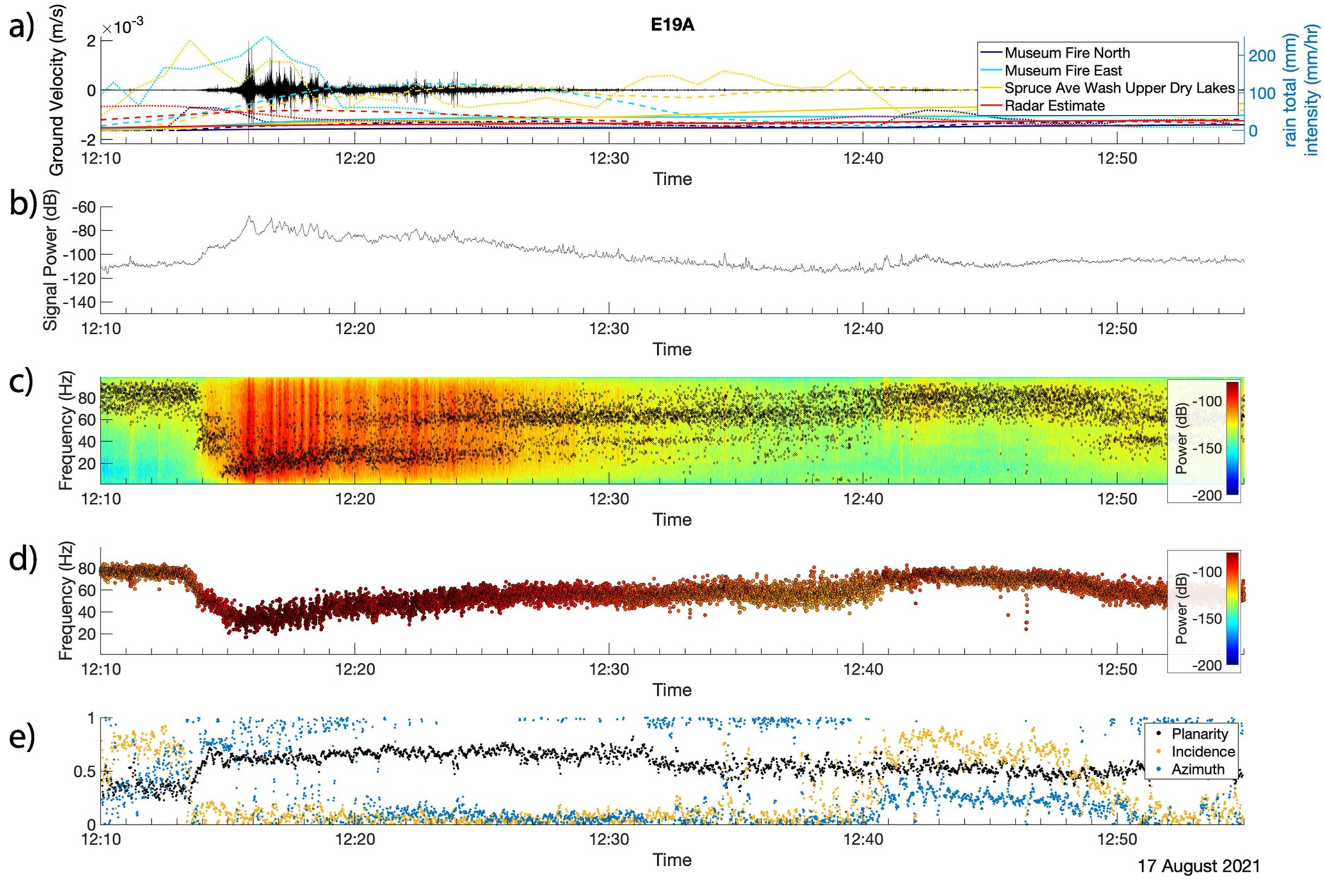

Figure 6. Seismic recording of debris flow at station E19A on 21 August 2021. Top panels are the same as Figure 5, except panel (a) amplitude scale.

installed ~90 m upstream recorded sediment transport (Figure 7). Photos were taken at 5 min intervals with an uncertainty of ~1 min on the timestamp. These images capture high intensity rainfall and sheet flow outside the channel prior to the debris flow, which is observed in the second image. Due to the uncertainty on the game photo timings and the difference in locations, we cannot precisely tie the photos directly to seismic observations. However, based on these timings, it seems probable we are observing sheet flow or similar in the initial higher frequency energy followed by sediment pulses (including downed trees) during the main flow, though further work is needed to confirm this.

Based on an analysis of multiple events recorded at station E19A, debris flows at this station are characterized by a low incidence angle, a high planarity, and an azimuth measurement oriented ~160° for most of the debris flows. This azimuth is the direction from the station to the nearest point in the channel; variations from this orientation may track the front of sediment pulses moving downstream. Polarization measurements at this station are more consistent than those observed at other stations, but in general, we observe consistent azimuths, moderate planarities and low incidence angles in debris flow signals regardless of the station.

Using the equations in Section 2, we generate synthetic models of signal power and spectral content for sources that include background noise, rainfall, and debris flow signals. For both debris flow and rain fall signals, the particle impact duration is shorter than the frequencies the seismometer can accurately measure. As such, observationally, the impacts are instantaneous. One result of this is that the frequency content is controlled by the Green's function and the distance between the source (rain or particle impacts) and the seismometer. In our modeling, we approximate the Green's function at the station by matching the frequency content of rain and the debris flows recorded at station E19A on 16 July 2021 (Figure 5). In the synthetic models, the station/channel distance and channel width were matched to the geometry observed at site E19A (Table S3 in Supporting Information S1). The seismometer is located 20 m from the channel, which is 2 m in width. In our synthetic models (Figure 8), we reproduce the initial high frequency signal associated with rain using a rainfall intensity of 100 mm/hr for the

Figure 7. Game camera images of the channel above E19A before and during the debris flow on 21 August 2021. Images were taken at 12:14 and 12:19 local time, respectively.

first 450 s of the signal. As the modeled debris flow approaches the station, we observe a decrease in f_{max} and f_{cent}, which occurs when the debris flow becomes the dominant signal. The subsequent increase in f_{max} and f_{cent} and the sawtooth patterns observed in the data are modeled using a sine function (Equation 13) to represent pulses of increased sediment size moving down the channel. In the observed data, this signal could represent a combination of increased grain size or flow velocity, which would produce similar signals. As this sine function decays, the f_{max} value becomes more stable and is consistent with the strongest seismic signal originating from the closest point in the channel to the seismometer. Finally, the decay in signal amplitude is produced by decreasing the grain size. This is a simplification of the process as the decay in amplitude observed in our recorded data is likely due to a combination of decrease in grain size, flow velocity, and flow volume. Over the 2021 monsoon season we record multiple debris flows at station E19A, which have similar signal power and frequency patterns. Based on field observations, we infer that there was one water-dominated flow during this season, which occurred on 25 July and had significant bedload data from this flow is shown in Supporting Information S1 (Figure S2). While the seismic observations from this event are similar to debris flows, the signal power is ~1/10 what was observed

Journal of Geophysical Research: Earth Surface 10.1029/2022JF006962

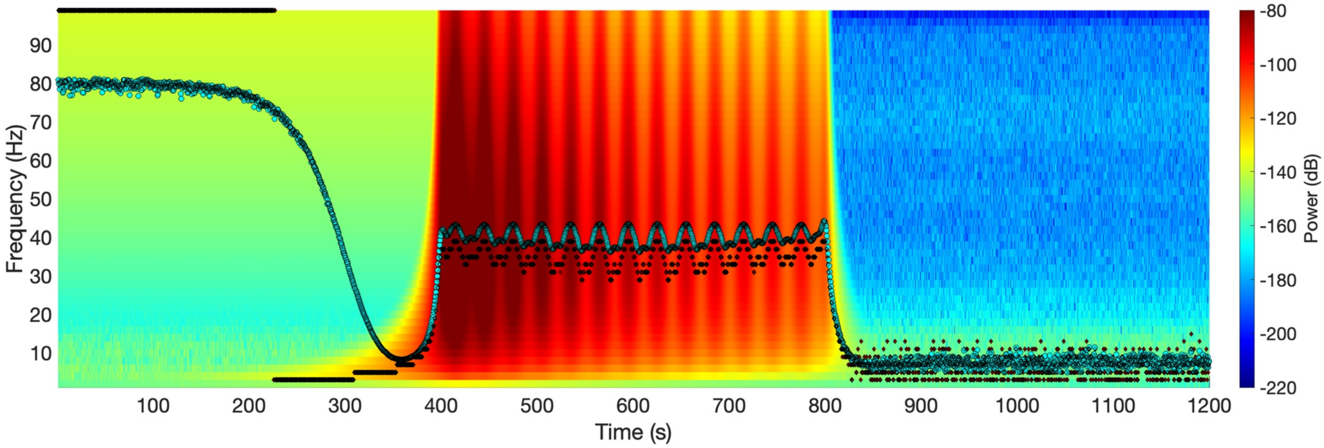

Figure 8. Spectrogram for synthetic debris flow model. Blue circles are spectral centroid (f_{cent}) and black diamonds are the frequency with the maximum energy (f_{max}).

during debris flows. This result is similar to what is expected from modeling (Figures S3 and S4 in Supporting Information S1).

Results from this work confirm the validity of theoretical models for understanding the seismic signals produced by post-fire debris flows. The highest amplitude observed in most flows appears to correspond with the snout passing by the station. Additional high-amplitude peaks are likely indicative of sediment or high velocity pulses within the flow passing by the station. The peak in signal power within these pulses occurs when the coarse sediment is in closest proximity to the station. The frequency content of debris flow is primarily controlled by the distance of the flow from the station. However, this frequency content can also provide insight into the behavior of a flow. The sawtooth pattern in frequency content (f_{max} and f_{cent}) observed during debris flow events is likely due to coarse sediment or high velocity pulses moving down the channel. Pulses with large grain sizes produce higher amplitude seismic signals; therefore, even when they are farther from the station than smaller-grain sized flows, they may still produce a large enough signal to lower the f_{max} and f_{cent} measurements. For a long flow with consistent grain size distribution and velocity, we would expect a signal with consistent frequency content. This is often observed empirically later in flows when the f_{max} measurements become consistent, likely indicating that the debris flow is no longer moving downslope in pulses or has evolved into a finer-grained or water-dominated flow. The f_{cent} measurement continues to change later in flows as the grain size decreases and there are less contributions from sediment transport further away in the channel to the recorded signal.

Debris flow velocity can be estimated by examining the frequency content of the seismic signal or the cross-correlation of signals between stations based on Equation 11. At station E19A, we estimate velocities of the debris flow's snout following Lai et al. (2018), who show that debris flow frequency content is controlled by the Green's function and source-flow distance. To accomplish this, we calculate $dP/df = 0$ for Equation 11 and solve for r using f_{max} as the input frequency. We then use the Pythagorean theorem to calculate the along-channel x location of the front of the flow, with r as the hypotenuse and r_0 and x as the legs. In this calculation, $x = 0$ at the point in the channel closest to the station. To calculate smoothed f_{max} values from our data, we remove points greater than 40 Hz, which are unlikely due to flow within the channel, and use bisquare robust regression to fit the observed f_{max} values as the flow approaches the station. A linear fit is used for simplicity in both estimating f_{max} and velocity. Using this approach, we estimate a velocity of ~5.1 m/s for the first debris flow that occurred on 16 July at 13:17:48 (Figure 9). Applying this to later pulses at 13:18:34 and 13:19:32 in the first 16 July event we estimate velocities that range from ~4.5 to 5.4 m/s. There is considerable uncertainty in these estimates as the velocity is highly dependent on the selected time window and the inputs used to estimate the Green's function. This is especially true for later measurements where there is increased noise in the signal.

The four stations used during the 2021 deployment did not allow us to measure debris flow velocities using cross correlation as we did not have multiple stations within any drainage in the upper watershed. However, we show an example from lower in the watershed downstream of where a majority of the coarse material was deposited (Figure 9). We filter signals between 1 and 40 Hz, normalize them, and then cross correlate the signal powers between stations COCB and CFSG, which were located ~1.2 km from each other along the channel (Figure 9).

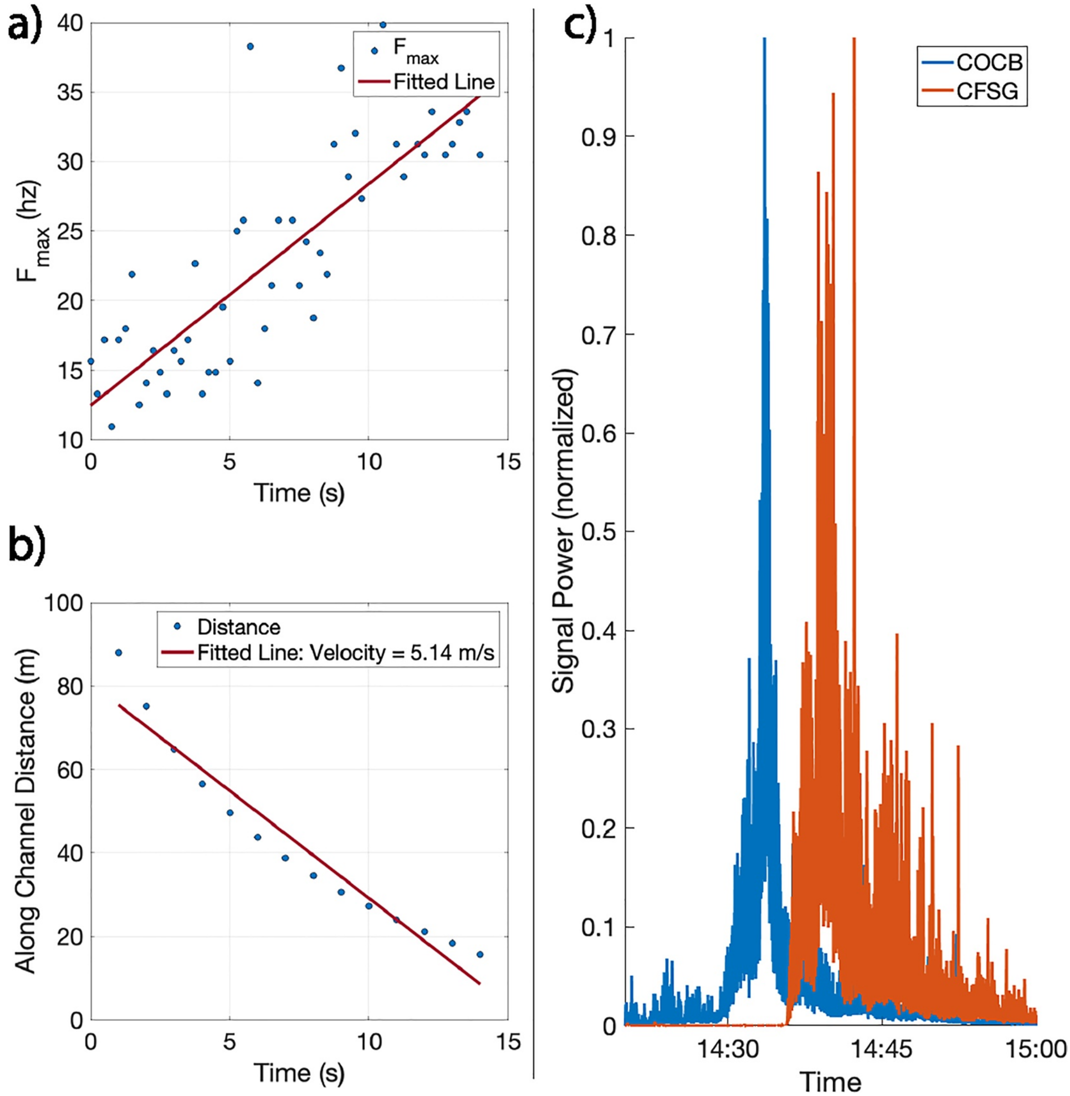

Figure 9. Debris flow velocity estimates. Panel (a) shows changes in f_{max} over time beginning at 13:17:48 on 16 July 2021 at station E19A. Red line is least-squares fit to the data. Panel (b) shows along channel distance of the debris flow snout calculated from f_{max} least squares fit in panel (a). Red line is fit to the data, slope of the red line is the velocity of the debris flow snout ~5.96 m/s. Panel (c) shows normalized signal power recorded at stations COCB and CFSG for an event on 13 July 2021. Cross correlating the signal results in a lag of 356 s between the two stations.

The lag time of the cross correlations for an event on 13 July 2021 was 356 s yielding an estimated velocity of 3.4 m/s for the flood in that reach of the channel. Applying this to multiple events over the summer led to velocity estimates between 2.6 and 4.1 m/s for the reach.

Constraining the Green's function at a station can present a challenge, especially in post-fire settings where stations are frequently deployed on steep unstable slopes and access may be limited due to hazards to personnel. However, if the rainfall rate is well-constrained by rain gauge data and the drop size distribution can be estimated, the frequency content and power of the rainfall seismic signal could provide a mechanism for calculating local high frequency Green's functions. Future work will explore methodologies for better calculating these Green's functions using rainfall data. Given that debris flows can alter the subsurface through scouring and deposition, an analysis of the rainfall may provide a mechanism for assessing these changes. Additionally, examining the frequency content of a debris flow signal can provide insight into the Green's function. The highest frequency f_{max} value associated with the debris flow will be observed when the debris flow is at the point in the channel that is in closest proximity to the station. If the distance between the station and the channel is known, this value can then be used as a constraint on the Green's function values. Though we do not attempt to replicate the signal exactly, the input values (geometry and Green's functions) for our forward model were selected to roughly match the signals and their frequency content produced by rainfall and debris flow at station E19A. The inputs and their rationales are presented in Supporting Information S1 (Table S3).

Initial results indicate that wave polarization may be a good differentiator between seismic sources in post-fire settings. At station E19A, the signal azimuth, calculated using Equation 4, is oriented toward the closest point in the channel to the station during debris flows. The signal associated with debris flows exhibits a higher planarity than other environmental events (i.e., wind, rain, lightning, etc.). The incidence angle is high during rain and low during debris flows, which may be related to the frequency content of the two signals. Work by Tsai and Atiganyanun (2014) shows that N_{jz} approaches unity at high frequencies while the amplitudes of horizontal components are diminished. Lower frequency surface waves have more energy on the horizontal components and less on the vertical. This is consistent with what we observe with rain ($f > 50$ Hz) and debris flows ($f > 5$ Hz).

Comparison to earthquakes and other energy sources affirms that debris flows produce a signal that is easily distinguishable from other sources of seismic energy even in sites hastily installed in suboptimal conditions (steep slopes, shallow burial etc.). Over the course of our monitoring, debris flows produce the highest amplitude signal observed in the 1–50 Hz frequency range. Additionally, the signal is much more emergent and has a longer duration than a typical earthquake signal. Based on these differences, automatic detection of events is achievable and could serve to help with early warning efforts.

4. Conclusions

In this study, we show data and interpretations for storms and debris flows recorded by seismic equipment in a post-fire setting. Results from this work affirm the validity of theoretical models of debris flow seismic energy generation and represent a step toward better characterizing changes in particles size and flow velocity using a single seismic station. Further, this work demonstrates the applicability of seismic monitoring for debris flow detection in this setting. Using seismic data, we are able to detect and distinguish seismic energy due to wind, lightning, rainfall, and debris flows/floods, demonstrating the efficacy of seismic data for event characterization and flood detection and early warning in these settings. Future work will build on this effort and better constrain and characterize post-fire debris flow behavior using seismic data.

Data Availability Statement

The data sets generated for this study can be found in the following online repositories: https://doi.org/10.7914/SN/1A_2019, https://www.flagstaff.az.gov/4111/Rainfalland-Stream-Gauge-Data. Data availability and access is described in detail in a data report on the project available here: https://doi.org/10.3389/feart.2021.649938. National Lightning Detection Network (NLDN) data were made available by Vaisala (https://www.vaisala.com/en/products/national-lightning-detection-network-nldn).

Acknowledgments

The funding for this project was provided by a National Science Foundation Grant: RAPID: Seismic Monitoring of Post-Fire Debris Flows Associated with the Museum Fire, Northern Arizona EAR 1946321, the US Department of Agriculture, Forest Service, Coconino National Forest (20-CS-11030400-101), the City of Flagstaff, AZ and Coconino County, AZ. The seismic instruments were provided by the Incorporated Research Institutions for Seismology (IRIS) through the PASSCAL Instrument Center at New Mexico Tech and by Northern Arizona University. Seismic data are available through the IRIS Data Management Center. The facilities of the IRIS Consortium are supported by the National Science Foundation's Seismological Facilities for the Advancement of Geoscience (SAGE) Award under Cooperative Support Agreement EAR-1851048. Thorough and constructive reviews by two anonymous reviewers and the associate editor greatly improved the quality of this manuscript. Author JL is employed by the company JE Fuller Hydrology and Geomorphology, Inc.

References

Abatzoglou, J. T., & Williams, A. P. (2016). Impact of anthropogenic climate change on wildfire across western US forests. *Proceedings of the National Academy of Sciences of the United States of America*, *113*(42), 11770–11775. https://doi.org/10.1073/pnas.1607171113

Adams, D. K., & Comrie, A. C. (1997). The North American monsoon. *Bulletin of the American Meteorological Society*, *78*(10), 2197–2213. https://doi.org/10.1175/1520-0477(1997)078<2197:tnam>2.0.co;2

Aki, K., & Richards, P. G. (2002). *Quantitative seismology* (2nd ed.). University Science Books.

Allstadt, K. (2013). Extracting source characteristics and dynamics of the August 2010 Mount Meager landslide from broadband seismograms. *Journal of Geophysical Research: Earth Surface*, *118*(3), 1472–1490. https://doi.org/10.1002/jgrf.20110

Allstadt, K. E., Farin, M., Iverson, R. M., Obryk, M. K., Kean, J. W., Tsai, V. C., et al. (2020). Measuring basal force fluctuations of debris flows using seismic recordings and empirical Green's functions. *Journal of Geophysical Research: Earth Surface*, *125*(9), e2020JF005590. https://doi.org/10.1029/2020jf005590

Atlas, D., & Ulbrich, C. W. (1977). Path- and area-integrated rainfall measurement by microwave attenuation in the 1–3 cm band. *Journal of Applied Meteorology*, *16*(12), 1322–1331. https://doi.org/10.1175/1520-0450(1977)016<1322:paairm>2.0.co;2

Bakker, M., Legout, C., Gimbert, F., Nord, G., Boudevillain, B., & Freche, G. (2022). Seismic modelling and observations of rainfall. *Journal of Hydrology*, *610*, 127812. https://doi.org/10.1016/j.jhydrol.2022.127812

Barnett, T. P., Adam, J. C., & Lettenmaier, D. P. (2005). Potential impacts of a warming climate on water availability in snow-dominated regions. *Nature*, *438*(7066), 303–309. https://doi.org/10.1038/nature04141

Barnett, T. P., Pierce, D. W., Hidalgo, H. G., Bonfils, C., Santer, B. D., Das, T., et al. (2008). Human-induced changes in the hydrology of the western United States. *Science*, *319*(5866), 1080–1083. https://doi.org/10.1126/science.1152538

Benson, R., Ahern, T., Trabant, C., Weertman, B., Casey, R., Stromme, S., & Karstens, R. (2012). Real time data for seismology at the IRIS data management center, AN Nsf-sponsored facility. In *AGU fall meeting abstracts* (pp. IN33C–1555).

Bessason, B., Eiríksson, G., Thorarinsson, Ó., Thórarinsson, A., & Einarsson, S. (2017). Automatic detection of avalanches and debris flows by seismic methods. *Journal of Glaciology*, *53*(182), 461–472. https://doi.org/10.3189/002214307783258468

Brown, T. J., Hall, B. L., & Westerling, A. L. (2004). The impact of twenty-first century climate change on wildland fire danger in the western United States: An applications perspective. *Climatic Change*, *62*(1–3), 365–388. https://doi.org/10.1023/b:clim.0000013680.07783.de

Burtin, A., Bollinger, L., Cattin, R., Vergne, J., & Nábělek, J. L. (2009). Spatiotemporal sequence of Himalayan debris flow from analysis of high-frequency seismic noise. *Journal of Geophysical Research: Earth Surface*, *114*(F4), 410–416. https://doi.org/10.1029/2008jf001198

Burtin, A., Bollinger, L., Vergne, J., Cattin, R., & Nábělek, J. L. (2008). Spectral analysis of seismic noise induced by rivers: A new tool to monitor spatiotemporal changes in stream hydrodynamics. *Journal of Geophysical Research: Solid Earth*, *113*(B5), 911–914. https://doi.org/10.1029/2007jb005034

Burtin, A., Cattin, R., Bollinger, L., Vergne, J., Steer, P., Robert, A., et al. (2011). Towards the hydrologic and bed load monitoring from high-frequency seismic noise in a braided river: The "torrent de St Pierre", French Alps. *Journal of Hydrology*, *408*(1–2), 43–53. https://doi.org/10.1016/j.jhydrol.2011.07.014

Burtin, A., Hovius, N., McArdell, B. W., Turowski, J. M., & Vergne, J. (2014). Seismic constraints on dynamic links between geomorphic processes and routing of sediment in a steep mountain catchment. *Earth Surface Dynamics*, *2*(1), 21–33. https://doi.org/10.5194/esurf-2-21-2014

Burtin, A., Hovius, N., Milodowski, D. T., Chen, Y.-G., Wu, Y.-M., Lin, C.-W., et al. (2013). Continuous catchment-scale monitoring of geomorphic processes with a 2-D seismological array. *Journal of Geophysical Research: Earth Surface*, *118*(3), 1956–1974. https://doi.org/10.1002/jgrf.20137

Cook, E. R., Woodhouse, C. A., Eakin, C. M., Meko, D. M., & Stahle, D. W. (2004). Long-term aridity changes in the western United States. *Science*, *306*(5698), 1015–1018. https://doi.org/10.1126/science.1101982

Cornet, E. S., Guillén, I. V., Khazaradze, G., Górriz, B. B., Bellavista, G. F. i., & Vilaplana, J. M. (2005). Seismic detection and characterization of landslides and other mass movements. *Natural Hazards and Earth System Sciences*, *5*(6), 791–798. https://doi.org/10.5194/nhess-5-791-2005

Coviello, V., Arattano, M., Comiti, F., Macconi, P., & Marchi, L. (2019). Seismic characterization of debris flows: Insights in to energy radiation and implications for warning. *Journal of Geophysical Research: Earth Surface*, *12*(4), 1440–1463. https://doi.org/10.1029/2018jf004683

Cummins, K. L., & Murphy, M. J. (2009). An overview of lightning locating systems: History, techniques, and data uses, with an in-depth look at the U.S. NLDN. *IEEE Transactions on Electromagnetic Compatibility*, *51*(3), 499–518. https://doi.org/10.1109/temc.2009.2023450

DeBano, L. F. (2000). The role of fire and soil heating on water repellency in wildland environments: A review. *Journal of Hydrology*, *231*, 195–206. https://doi.org/10.1016/s0022-1694(00)00194-3

Ekstrom, G., & Stark, C. P. (2013). Simple scaling of catastrophic landslide dynamics. *Science*, *339*(6126), 1416–1419. https://doi.org/10.1126/science.1232887

Farin, M., Tsai, V. C., Lamb, M. P., & Allstadt, K. E. (2019). A physical model of the high-frequency seismic signal generated by debris flows. *Earth Surface Processes and Landforms*, *44*(13), 2529–2543. https://doi.org/10.1002/esp.4677

Gimbert, F., Tsai, V. C., & Lamb, M. P. (2014). A physical model for seismic noise generation by turbulent flow in rivers. *Journal of Geophysical Research: Earth Surface*, *119*(10), 2209–2238. https://doi.org/10.1002/2014jf003201

Holm, R. F. (1988). *Geologic map of San Francisco Mountain, Elden Mountain, and Dry Lake Hills, Coconino County, Arizona*. United State Geological Survey. Retrieved from https://pubs.er.usgs.gov/publication/i1663

Johnson, C. W., Meng, H., Vernon, F., & Ben-Zion, Y. (2019). Characteristics of ground motion generated by wind interaction with trees, structures, and other surface obstacles. *Journal of Geophysical Research: Solid Earth*, *124*(8), 8519–8539. https://doi.org/10.1029/2018jb017151

Jolly, W. M., Cochrane, M. A., Freeborn, P. H., Holden, Z. A., Brown, T. J., Williamson, G. J., & Bowman, D. M. J. S. (2015). Climate-induced variations in global wildfire danger from 1979 to 2013. *Nature Communications*, *6*(1), 7537. https://doi.org/10.1038/ncomms8537

Jones, J. P., Eaton, D. W., & Caffagni, E. (2016). Quantifying the similarity of seismic polarizations. *Geophysical Journal International*, *204*(2), 968–984. https://doi.org/10.1093/gji/ggv490

Jurkevics, A. (1988). Polarization analysis of three-component array data. *Bulletin of the Seismological Society of America*, *78*(5), 1725–1743.

Jurwitz, L. R. (1953). Arizona's two-season rainfall pattern. *Weatherwise*, *6*(4), 96–99. https://doi.org/10.1080/00431672.1953.9932951

Kean, J. W., Coe, J. A., Coviello, V., Smith, J. B., McCoy, S. W., & Arattano, M. (2015). Estimating rates of debris flow entrainment from ground vibrations. *Geophysical Research Letters*, *42*(15), 6365–6372. https://doi.org/10.1002/2015gl064811

Kean, J. W., & Staley, D. M. (2011). Direct measurement of the hydrologic conditions leading up to and during post-fire debris flow in southern California, USA. In R. Genevois, D. L. Hamilton, & A. Prestininzi (Eds.), *Debris-flow hazards mitigation, mechanics, prediction, and assessment* (pp. 685–694). Casa Editrice University La Sapienza.

Lai, V. H., Tsai, V. C., Lamb, M. P., Ulizio, T. P., & Beer, A. R. (2018). The seismic signature of debris flows: Flow mechanics and early warning at Montecito, California. *Geophysical Research Letters*, *45*(11), 5528–5535. https://doi.org/10.1029/2018gl077683

Marineau, M. D., Wright, S. A., Gaeuman, D., Curran, C. A., Stark, K., Siemion, J., & Schenk, E. R. (2019). Overview of five recent acoustic bedload monitoring field experiments using hydrophones, in Sediment surrogate measurements, sediment yield and fingerprinting, stream restoration, water quality, watershed management, v. 4 of Proceedings of SEDHYD 2019. In *Conferences on sedimentation and hydrologic modeling* (p. 14).

Marshall, J. S., Langille, R. C., & Palmer, W. M. K. (1947). Measurement of rainfall by radar. *Journal of Meteorology*, *4*(6), 186–192. https://doi.org/10.1175/1520-0469(1947)004<0186:morbr>2.0.co;2

McGuire, L. A., Rengers, F. K., Kean, J. W., Staley, D. M., & Mirus, B. B. (2018). Incorporating spatially heterogeneous infiltration capacity into hydrologic models with applications for simulating post-wildfire debris flow initiation. *Hydrological Processes*, *32*(9), 1173–1187. https://doi.org/10.1002/hyp.11458

McGuire, L. A., & Youberg, A. M. (2020). What drives spatial variability in rainfall intensity-duration thresholds for post-wildfire debris flows? Insights from the 2018 Buzzard Fire. *Landslides*, *17*(10), 2385–2399. https://doi.org/10.1007/s10346-020-01470-y

Michel, A., Kean, J. W., Smith, J. B., Allstadt, K. E., & Coe, J. A. (2019). Taking the pulse of debris flows: Extracting debris-flow dynamics from good vibrations in southern California and central Colorado. In *7th international conference on debris-flow hazards mitigation* (p. 8).

Murphy, M. J., Cramer, J. A., & Said, R. K. (2021). Recent history of upgrades to the U.S. national lightning detection network. *Journal of Atmospheric and Oceanic Technology*, *38*(3), 573–585. https://doi.org/10.1175/jtech-d-19-0215.1

Museum Fire BAER Team. (2019). Museum fire burned area emergency response (BAER) executive summary.

Nauslar, N. J., Hatchett, B. J., Brown, T. J., Kaplan, M. L., & Mejia, J. F. (2019). Impact of the North American monsoon on wildfire activity in the southwest United States. *International Journal of Climatology*, *39*(3), 1539–1554. https://doi.org/10.1002/joc.5899

Orville, R. E. (2008). Development of the national lightning detection network. *Bulletin of the American Meteorological Society*, *89*(2), 180–190. https://doi.org/10.1175/bams-89-2-180

Parks, S. A., Miller, C., Parisien, M.-A., Holsinger, L. M., Dobrowski, S. Z., & Abatzoglou, J. (2015). Wildland fire deficit and surplus in the western United States, 1984–2012. *Ecosphere*, *6*(12), art275–13. https://doi.org/10.1890/es15-00294.1

Porter, R., Joyal, T., Beers, R., Loverich, J., LaPlante, A., Spruell, J., et al. (2021). Seismic monitoring of post-wildfire debris flows following the 2019 Museum Fire, Arizona. *Frontiers in Earth Science*, *9*, 649938. https://doi.org/10.3389/feart.2021.649938

Radeloff, V. C., Helmers, D. P., Kramer, H. A., Mockrin, M. H., Alexandre, P. M., Bar-Massada, A., et al. (2018). Rapid growth of the US wildland-urban interface raises wildfire risk. *Proceedings of the National Academy of Sciences of the United States of America*, *115*(13), 3314–3319. https://doi.org/10.1073/pnas.1718850115

Raymond, C. A., McGuire, L. A., Youberg, A. M., Staley, D. M., & Kean, J. W. (2020). Thresholds for post-wildfire debris flows: Insights from the Pinal Fire, Arizona, USA. *Earth Surface Processes and Landforms*, *45*(6), 1349–1360. https://doi.org/10.1002/esp.4805

Roth, D. L., Brodsky, E. E., Finnega, N., Rickenmann, D., Turowski, J., & Badoux, A. (2016). Bed load sediment transport inferred from seismic signals near a river. *Journal of Geophysical Research: Solid*, *121*(121), 725–747. https://doi.org/10.1002/2015jf003782

Roth, D. L., Finnegan, N. J., Brodsky, E. E., Cook, K. L., Stark, C. P., & Wang, H. W. (2014). Migration of a coarse fluvial sediment pulse detected by hysteresis in bedload generated seismic waves. *Earth and Planetary Science Letters*, *404*(C), 144–153. https://doi.org/10.1016/j.epsl.2014.07.019

Sankey, J. B., Kreitler, J., Hawbaker, T. J., McVay, J. L., Miller, M. E., Mueller, E. R., et al. (2017). Climate, wildfire, and erosion ensemble foretells more sediment in western USA watersheds. *Geophysical Research Letters*, *44*(17), 8884–8892. https://doi.org/10.1002/2017gl073979

Schenk, E. R., Schiefer, E., Young, E., & Helton, C. (2021). Surface water hydrology and flood recurrence in the Flagstaff, Arizona area, 2008-2019. City of Flagstaff Technical Report. 91. https://doi.org/10.4211/hs.8da8bb7cb66d475ea03af1a79b38a446

Schmandt, B., Aster, R. C., Scherler, D., Tsai, V. C., & Karlstrom, K. (2013). Multiple fluvial processes detected by riverside seismic and infrasound monitoring of a controlled flood in the Grand Canyon. *Geophysical Research Letters*, *40*(18), 4858–4863. https://doi.org/10.1002/grl.50953

Staley, D. M., Kean, J. W., & Rengers, F. K. (2020). The recurrence interval of post-fire debris-flow generating rainfall in the southwestern United States. *Geomorphology*, *370*, 107392. https://doi.org/10.1016/j.geomorph.2020.107392

Steel, Z. L., Safford, H. D., & Viers, J. H. (2015). The fire frequency-severity relationship and the legacy of fire suppression in California forests. *Ecosphere*, *6*(1), 1–23. https://doi.org/10.1890/es14-00224.1

Stempniewicz, V. A. (2014). *Evaluating erosion risk mitigation due to forest restoration treatments using alluvial chronology and hydraulic modeling*. Northern Arizona University.

Suwa, H., Okano, K., & Kanno, T. (2011). Forty years of debris-flow monitoring at Kamikamihorizawa Creek, Mount Yakedake, Japan. *Italian Journal of Engineering Geology and Environment*, 605–613. https://doi.org/10.4408/ijege.2011-03.b-066

Tang, H., McGuire, L. A., Rengers, F. K., Kean, J. W., Staley, D. M., & Smith, J. B. (2019). Evolution of debris-flow initiation mechanisms and sediment sources during a sequence of postwildfire rainstorms. *Journal of Geophysical Research: Earth Surface*, *124*(6), 1572–1595. https://doi.org/10.1029/2018jf004837

Touma, D., Stevenson, S., Swain, D. L., Singh, D., Kalashnikov, D. A., & Huang, X. (2022). Climate change increases risk of extreme rainfall following wildfire in the western United States. *Science Advances*, *8*(13), eabm0320. https://doi.org/10.1126/sciadv.abm0320

Trabant, C., Stromme, S., & Weertman, B. (2008). Managing a torrent of diverse low-latency data streams at the IRIS DMC. In *AGU fall meeting abstracts* (pp. G43A–G0666).

Tsai, V. C., & Atiganyanun, S. (2014). Green's functions for surface waves in a generic velocity StructureShort note. *Bulletin of the Seismological Society of America*, *104*(5), 2573–2578. https://doi.org/10.1785/0120140121

Tsai, V. C., Minchew, B., Lamb, M. P., & Ampuero, J.-P. (2012). A physical model for seismic noise generation from sediment transport in rivers. *Geophysical Research Letters*, *39*(2), L02404. https://doi.org/10.1029/2011gl050255

Uijlenhoet, R., & Stricker, J. N. M. (1999). A consistent rainfall parameterization based on the exponential raindrop size distribution. *Journal of Hydrology*, *218*(3–4), 101–127. https://doi.org/10.1016/s0022-1694(99)00032-3

Vidale, J. E. (1986). Complex polarization analysis of particle motion. *Bulletin of the Seismological Society of America*, *76*(5), 1393–1405.

Visual Crossing Corporation. (2021). Visual crossing weather. Retrieved from https://www.visualcrossing.com/

Walter, F., Burtin, A., McArdell, B. W., Hovius, N., Weder, B., & Turowski, J. M. (2017). Testing seismic amplitude source location for fast debris-flow detection at Illgraben, Switzerland. *Natural Hazards and Earth System Sciences*, *17*(6), 939–955. https://doi.org/10.5194/nhess-17-939-2017

Westerling, A. L. (2016). Increasing western US forest wildfire activity: Sensitivity to changes in the timing of spring. *Philosophical Transactions of the Royal Society B: Biological Sciences*, *371*(1696), 20150178. https://doi.org/10.1098/rstb.2015.0178

Westerling, A. L., Gershunov, A., Brown, T. J., Cayan, D. R., & Dettinger, M. (2003). Climate and wildfire in the western United States. *Bulletin of the American Meteorological Society*, *84*(5), 595–604. https://doi.org/10.1175/bams-84-5-595

Westerling, A. L., Hidalgo, H. G., Cayan, D. R., & Swetnam, T. W. (2006). Warming and earlier spring increase western U.S. Forest wildfire activity. *Science*, *313*(5789), 940–943. https://doi.org/10.1126/science.1128834

Yue, X., Mickley, L. J., Logan, J. A., & Kaplan, J. O. (2013). Ensemble projections of wildfire activity and carbonaceous aerosol concentrations over the western United States in the mid-21st century. *Atmospheric Environment*, *77*, 767–780. https://doi.org/10.1016/j.atmosenv.2013.06.003

Zhang, Z., Walter, F., McArdell, B. W., Haas, T., Wenner, M., Chmiel, M., & He, S. (2021). Analyzing bulk flow characteristics of debris flows using their high frequency seismic signature. *Journal of Geophysical Research: Solid Earth*, *126*(12), e2021JB022755. https://doi.org/10.1029/2021jb022755

References From the Supporting Information

Iverson, R. M. (1997). The physics of debris flows. *Reviews of Geophysics*, *35*(3), 245–296. https://doi.org/10.1029/97rg00426